Journal of Atmospheric Chemistry **41:** 211–237, 2002.

Three-Dimensional Calculation of Photolysis Frequencies in the Presence of Clouds and Impact on Photochemistry

A-L. BRASSEUR [1], R. RAMAROSON [1], A. DELANNOY [1], W. SKAMAROCK [2] and M. BARTH [2]

[1] *ONERA – DMPH/EAG, BP 72, 92322 Châtillon, France, e-mail: al.brasseur@onera.fr*
[2] *NCAR/MMM, Boulder, CO 80307, U.S.A.*

(Received: 10 November 2000; in final form: 27 June 2001)

Abstract. For atmospheric photochemistry, clouds can significantly affect actinic flux distributions. In this paper, we examine the effects of convective clouds on the three-dimensional distribution of the spectral actinic flux and on photolysis frequencies for various chemical species. Three-dimensional solutions of the UV-VIS radiative transfer equation are produced using the Spherical Harmonic Discrete Ordinary Method solution technique. This solver uses as input the 3-D cloud characteristics simulated by a dynamical cloud model. The ultraviolet and visible spectra are divided into 5 intervals in order to explore the wavelength dependency of the cloud effect on the actinic flux. Results show that the distribution of the actinic flux over the cloud domain is far from homogeneous and depends primarily on the cloud extinction associated with the hydrometeors. Maximum actinic flux is found at the top edge of the cloud and is related to scattering by ice crystals. The actinic flux is enhanced by a factor of 2 to 5, compared to clear air values, above, at the top edge, and around the cloud. The 3-D actinic flux is used to calculate the photolysis rates for some chemical species (e.g. NO_2, O_3, and HCHO). For computing photolysis rates, a discretized spectral representation of the absorption wavelengths is used in the model. The calculated photolysis rates are distributed inhomogeneously throughout the cloud, and maxima are found in regions where the actinic flux is enhancement is large. Temperature effects on absorption are found in the photolysis frequencies of some species. Finally, the potential importance of this photolysis enhancement on photochemistry is studied using box model simulations. Results show that enhanced OH concentrations are found in the upper troposphere (120–200%) over the clouds and changes in ozone production rates (+15%) are obtained in quasi-steady state conditions.

Key words: actinic flux, clouds , OH, O_3, photolysis frequencies.

1. Introduction

Photodissociation of major tropospheric species is the driving force for atmospheric daylight chemistry. In general, this photochemistry produces odd hydrogen radicals (HO_x), which readily react with source gases, e.g., hydrocarbons, carbon monoxide, odd nitrogen species (NO_y), and halogen species. The photodissociation frequency of any species depends upon the spectral actinic flux, that

is, the flux of solar radiation that reaches the molecule. As the solar flux goes through the earth's atmosphere it can be modified by several factors. For example, photolysis reactions in the upper and middle atmosphere remove the solar flux of small wavelengths (<290 nm). Another important way to modify the actinic flux is through scattering of the photons by the earth's surface, other molecules, aerosols, and clouds. In this study we show how the three-dimensional character of cumulonimbus clouds modify the actinic flux in a heterogeneous manner and discuss the importance of this altered flux on photolysis frequencies and ultimately tropospheric chemistry in the upper troposphere and lower stratosphere (UT/LS).

Observations confirm that clouds have a large impact on radiative energy flows in the atmosphere (Raïsänen *et al.*, 1999; Valero *et al.*, 1999; Josefsson and Landelius, 2000; Matthijsen *et al.*, 2000) and consequently on photolysis frequencies (Kelley *et al.*, 1995; Los *et al.*, 1997; Crawford *et al.*, 1999). In the troposphere, thick and layered clouds are regularly observed. It has been shown by observations that the presence of high and mid-level thick cirrus and altocumulus clouds implies an enhancement of the available solar flux above the clouds, and the difference from clear sky conditions can be important (Kelley and Dickerson, 1995; Trautmann *et al.*, 1999; Valero *et al.*, 1999; Shetter *et al.*, 1999).

In this work, we investigate the role of clouds on the repartitioning of actinic flux in a cloudy environment and on the photolysis rates of various tropospheric molecules. We use a simulation of deep convective storm clouds for the 10 July 1996 STERAO storm (Stratospheric-Tropospheric Experiment: Radiation, Aerosols and Ozone/Deep Convection experiment; Skamarock *et al.*, 2000) to study the potential role of convective clouds on photolysis rates. Sensitivity studies using a chemistry box model are conducted to highlight the importance of determining accurate photolysis frequencies for ozone, NO_x, and HO_x chemistry. The removal of transport processes in the box model allows for a clearer examination of the contribution of photolysis under cloudy conditions.

2. The 10 July 1996 STERAO Storm Simulation

The cloud fields used in this study are taken from a simulation of the 10 July STERAO storm produced by the nonhydrostatic cloud model COMMAS (COllaborative Model for MultiscaleAtmospheric Simulation). In Skamarock *et al.* (2000), detailed observations are compared with the cloud model simulation for this storm. The comparison shows that the simulation captures the general evolution of the observed storm from multicellular to supercellular structure, and the simulated storm compares reasonable well with the observed storm with respect to depth of the convective cells and stratiform region and the overall size of the storm.

In this study, we use the simulated fields from a single time in the simulation during the storm's multicellular stage to examine the radiative impact of the hydrometeor fields produced by the convection. A 3-D depiction of the hydrometeor fields at 3600 s in the simulation is shown in Figure 1. Three active convective cells

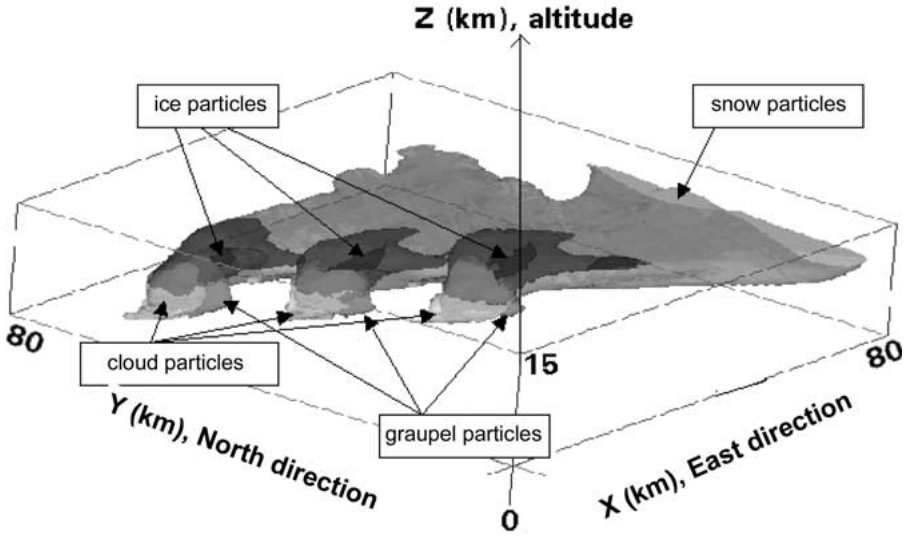

Figure 1. 3-D representation of the simulated deep convective cloud for 10 July 1996 (cumulonimbus).

can be discerned feeding an anvil that is expanding to the east/southeast. Figures 2 and 3, corresponding to horizontal and vertical cross sections used in the radiation analyses presented later in this paper, illustrate that the anvil is composed of snow and ice crystals, while the cores are a mixture of cloud drops, snow, and hail.

For the radiation calculations, the gridded cloud model hydrometeor fields are used. The cloud model simulation uses a vertical grid spacing that varies from 50 m at the surface to 700 m above 10 km, with 50 levels used in a 20 km deep domain. The horizontal domain spanned 120 by 120 km (x, y) with a horizontal grid resolution of 1 km. COMMAS used the ice microphysics from the Goddard Cumulus Ensemble Model described in Tao and Simpson (1993). The size distributions of rain droplets, snow, and graupel/hail are parameterized as inverse exponential of the particle diameter (Tao and Simpson, 1993). The scalar quantities in the model, including the mixing ratios of the water species (vapor, cloud water, rain, ice, snow and hail), are advected using a modified Van-Leer type scheme that is monotonic (Wicker and Wilhemson, 1995).

3. Description of the Radiative Transfer Model

Turco (1975), Madronich (1987, 1990) and Van Weele (1995) have discussed in detail the importance of the actinic flux in the earth's atmosphere photochemistry. We summarize here the theory of actinic flux and the physical significance of the radiative terms considered by Madronich (1987) and radiative implications on the dissociation of air molecules.

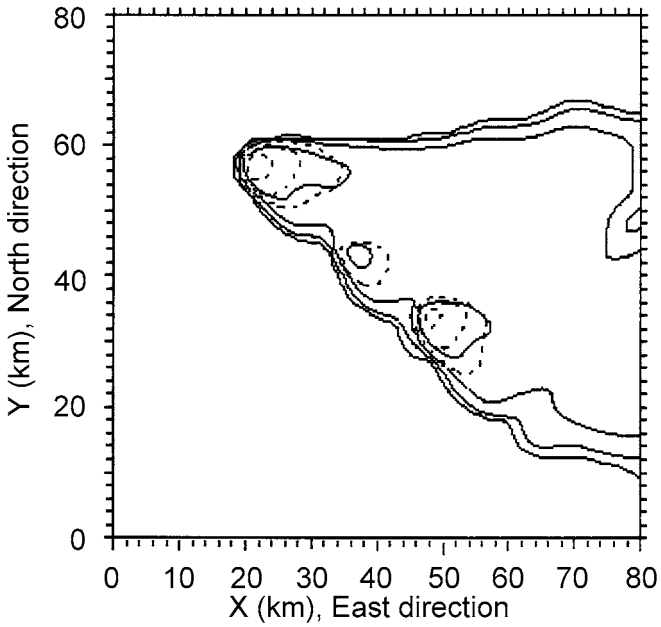

Figure 2. Hydrometeor mixing ratios at $z = 10.6$ km.

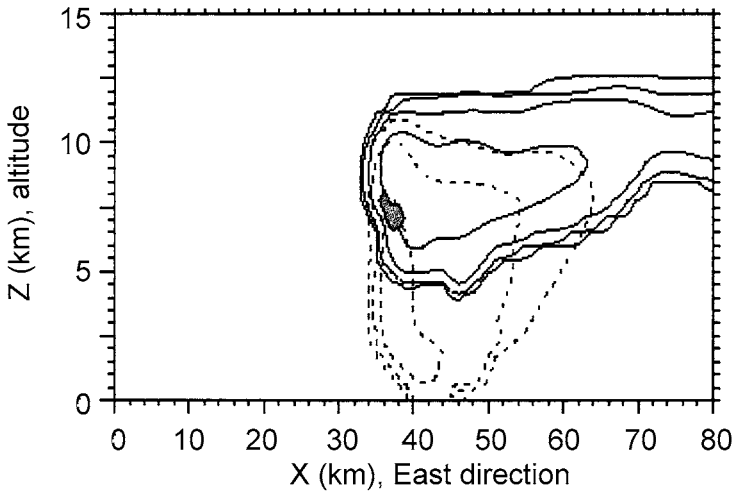

Figure 3. Hydrometeor mixing ratios at $y = 40$ km.

In the calculation of photolysis rates, Madronich (1987) pointed out the importance of differentiating between the irradiance, which is 'the flow of energy throughout the atmosphere' that can be measured across a plane, from the actinic flux, which is the flux of energy upon a sphere. In fact, the irradiance describes the flow of radiant energy through the atmosphere, while the actinic flux concerns the probability of an encounter between a photon and a molecule. Irradiance is

usually used to calculate the cloud heating rates and the actinic flux to evaluate the photodissociation of molecules.

The photodissociation coefficient, J_i, of a species, i, is defined by:

$$J_i = \int \phi_i(\lambda)\sigma_i(\lambda) \int_\theta \int_\varphi L(\lambda, \theta, \varphi) \sin\theta d\theta d\varphi d\lambda \,, \tag{1}$$

where $\phi_i(\lambda)$ is the quantum yield of species i at the wavelength λ; $\sigma_i(\lambda)$ is the absorption cross-section of species i at the wavelength λ; $L(\lambda, \theta, \varphi)$ is the spectral radiance or solar intensity (Chandrasekhar, 1960).

The spectral actinic flux, $F(\lambda)$, is determined as

$$F(\lambda) = \int_\theta \int_\varphi L(\lambda, \theta, \varphi) \sin\theta d\theta d\varphi \,. \tag{2}$$

The irradiance $E(\lambda)$ is the radiant energy transported from all directions across a surface (per unit time, per unit surface, per unit wavelength). $E(\lambda)$ is defined by:

$$E(\lambda) = \int_\theta \int_\varphi L(\lambda, \theta, \varphi) \cos\theta \sin\theta d\theta d\varphi \,, \tag{3}$$

where φ is the azimuth angle of the sun, θ is the solar zenith angle, and λ is the wavelength.

The factor $\cos\theta$ reflects the change in the projected area of the surface as the angle of incidence is varied. As the angle of incidence is changed from overhead to nearly glancing, the energy (irradiance) incident upon the layer decreases, but the actinic flux and photolysis frequencies remain unchanged. The irradiance and the actinic flux, although different, are closely related. They have the same units: photon.cm^{-2}.s^{-1}.nm^{-1}. In the atmosphere, irradiance is the radiometric quantity measured and to estimate the actinic flux the effects of the $\cos\theta$ are considered.

The actinic flux is the quantity appropriate for photolysis frequencies calculations.

3.1. DESCRIPTION OF THE SHDOM SOLVER

To determine the distribution of the spectral actinic flux, it is necessary to solve the radiative transfer equation numerically in the entire 3-D domain. We use the Spherical Harmonic Discrete Ordinate method (SHDOM) to solve the radiative transfer equation for a cloudy atmosphere. SHDOM is a solver developed by Evans (1998) and is summarized here. The differential form of the radiative transfer equation for the radiance $L(s)$ in the direction of a ray at a distance s along the ray can be written as:

$$\frac{dL(s)}{ds} = -k(L - J) \,, \tag{4}$$

where k is the volume extinction coefficient. J is the source function of the radiative transfer equation which is solved by SHDOM. The radiative transfer equation

is integrated for each of the discrete angles assuming that the source function field is fixed during the integration. The transform from spherical harmonics to discrete angles produces the source function $J(\mathbf{x}_i, \mu_j, \phi_k)$ at the gridpoint locations $\mathbf{x}_i$ for angles (μ_j, ϕ_k).

SHDOM is used to calculate the repartitioning of the solar flux at each grid point in the 3-dimensional domain by solving equations with two unknown variables L and J. As it was mentioned before, solutions can be obtained for monochromatic or spectral large-band radiation. We summarize here the iterative step developed by Evans, 1998:

- Step 1: A regular grid resolution is defined using a first guess for all variables, e.g. initializing the source function at each grid point. The resolution is 1 km × 1 km horizontally and 40 levels vertically (0–50 km). The horizontal boundary conditions are open.
- Step 2: The spherical harmonics source function J is transformed to discrete ordinates and (4) is integrated.
- Step 3: Radiance (L) from (4) is transformed to spherical harmonics.
- Step 4: Compute again source function and iterate on step 1.

These equations are iteratively solved until a convergence criterion is reached. When the iterations do not converge, the spatial grid is refined (stretched) in regions where the source function exhibits sharp spatial gradients across a cell.

Once the solution to Equations (3) and (4) are found, equation (2) is integrated to determine the spectral actinic flux.

The Rayleigh scattering is included in the calculations by feeding the appropriate scattering cross section and phase functions to SHDOM. The atmospheric particles responsible for scattering cover a range of sizes from gas molecules ($\approx 10^{-8}$ cm) to large raindrops and hail particles ($\approx$ cm). The relative intensity of the scattered light depends on the ratio of the particle size to the wavelength of the incident radiation. When this ratio is small, the scattered light is distributed equally into the forward and backward directions. When the particles are large, this is the case of the Mie scattering.

SHDOM uses the notion of Rayleigh coefficient, C_R. It is defined to be only wavelength dependent:

$$C_R = \frac{32\pi^3}{3\lambda^4} \frac{(n_0 - 1)^2 T_0}{N_0 P_0}$$

with $T_0 = 273$ K, $P_0 = 1013$ hPa and $N_0 = 2.687\ 10^{-19}$ cm^{-3}; n_0 is the air refraction index.

C_R values vary from 2.18×10^{-1} K.km^{-1}.hPa^{-1} for 200 nm to 4.13×10^{-3} K.km^{-1}.hPa^{-1} for 500 nm.

The expanded phase function, the cloud extinction, the single-scattering albedo, the temperature, and the concentration of ozone are calculated and tabulated over

the grid domain of the simulated cloud and are used as prescribed input parameters in SHDOM.

3.2. RADIATION PROPERTIES FOR VARIOUS CLOUD CHARACTERISTICS

The calculation of photolysis frequencies requires the solution of the radiative transfer equation in 3-D (Liou, 1980) including multiple scattering by air molecules and particles. Many simplified radiative models have been developed and used in the past for global models under clear sky conditions (e.g., Isaksen, 1977).

When clouds are present in the troposphere, they need to be taken into account. Water droplets, snow, precipitating droplets, graupel or hail, and ice crystals with different shapes can compose a cloud. Mie scattering can be applied for spherical droplets. However, for a polydispersed cloud the theory can be more complicated. For ice crystals, where usually diameters are larger than the scattered wavelength and shapes are not spherical, light is scattered preferentially forward along 3 directions. These highly variable cloud characteristics (i.e. concentration, distribution, size, type of particles, and shape) lead to a complex solution procedure for the radiative transfer due to different scattering for each particle type.

Using the cloud microphysics simulated by COMMAS, the radiative characteristics of each particle type and their optical properties are tabulated for SHDOM. The COMMAS model predicts 6 categories of water – vapor, cloud water, rain water, ice, snow, and graupel (see Tao and Simpson, 1993). For the 10 July 1996 STERAO simulation, graupel characteristics were set for hail (hail density $\rho_h = 0.9$ g cm^{-3} and hail number concentration $No = 4 \times 10^4$ m^{-4}).

For the SHDOM solver, liquid particles are considered spherical and thus their diffusion properties can be calculated with Mie theory. The distribution of cloud water drops is assumed to be a gamma-type, with an integral total number density of 300 particles/cm^3:

$$n(r) = C\, r^{\alpha}\, e^{=\beta r}\ (\alpha = 7)\,,$$

where $n(r)$ is the concentration of particles with a radius r; β (km^{-1}) is the extinction coefficient ; α and β define the distribution. The diffused light quantity is proportional to Cr^2. The mean effective radius is defined by the relation:

$$R_{\text{eff}} = \frac{\int r^3 n(r) dr}{\int r^2 n(r) dr} = \frac{\alpha + 3}{\beta}\,;$$

the distribution is defined by the total concentration, α and R_{eff}.

Mie theory describes the solar radiation in and around a distribution of spherical cloud water droplets, where the index of refraction for the liquid water cloud is required. In the ultraviolet band and in the visible, the index of refraction is constant whereas in the infrared region, the variation is wavelength dependent. The phase

function is tabulated using a spectral expansion (up to 1000 coefficients) for effective radii varying between 2 and 16 μm with a radius step of 2 μm. Cloud extinction is calculated as a function of the liquid water content and effective radius.

The parameterization of the radiative characteristics of ice crystals and its implication on the multiple scattering have been addressed by Takano and Liou (1989) and Liou and Rao (1996). For ice crystals, the distribution and the shape of particles are the main factors which determine multiple scattering characteristics. The assumption of considering ice crystals as sphere-equivalent with some effective radius is not suitable for the simulation of multiple scattering in presence of ice (see Sun and Shine, 1993). For this reason, in our simulations, we adopt the parameterization of the ice crystal radiative characteristics (phase function tabulated for any discrete scattering angles) proposed by Takano and Liou (1989). We apply these characteristics to both the ice and snow hydrometeor fields from the convective simulation. The extinction dependence versus ice water content is prescribed according to Platt (1997). The hexagonal structure of ice crystals is important for the determination of the bi-directional reflectance, albedo, and transmittance within the ice cloud, hence for the correct calculation of the distribution of scattered light within and around inhomogeneous clouds.

Graupel and rain are particles with diameters larger than the scattered wavelengths, and the extinction coefficients are approximated as a function of the liquid water content, or ice water content for graupel, and the effective radius of the specified hydrometeor. The phase functions of these particles are calculated using the Heyney-Greenstein approximation (expanded with an asymmetry factor equal to 0.87). It should be noted that because the population of graupel and rain are, for the same Liquid Water Content (LWC), less concentrated than for the smaller particles, multiple scattering is less efficient for these hydrometeors.

4. Results

The cloud shapes and radiative characteristics defined previously are used as input for SHDOM. The incoming spectral flux at the model top is assumed to be unity and results are presented in terms of an enhancement factor (EF) of the local spectral actinic flux relative to the incoming flux.

In order to highlight and discuss the role of clouds on the actinic flux in the troposphere and the lower stratosphere, calculations have been performed for clear sky and cloudy sky conditions. For each simulation, the effect of varying solar zenith angles (θ) is also studied. Only 0°, 45° and 60° are shown here. For this period of the year (10 July) and for the location studied here (northeastern Colorado), zenith angles less than 20° are not realistic because convection typically occurs in the late afternoon and early evening when zenith angles are larger. We stress that the scope of this paper is to study and highlight the cloud effects on photolysis frequencies in a cloudy atmosphere under various conditions, and we

are not attempting to reproduce the radiation distribution of the observed storm; radiation observations for this storm are sparse and their usefulness is limited.

In the presence of clouds, the multiple scattering of different wavelengths from 300 to 500 nm may have a different behavior. Based on the spectral band absorption of key molecules ($J(O^1D)$, $J(NO_2$, J(HCHO), $J(H_2O_2)$) in the lower stratosphere and the upper troposphere, the visible and UV radiation are divided in spectral bands defined by:

Band 1: 116–310 nm (center = 300 nm)

Band 2: 315–330 nm (center = 320 nm)

Band 3: 335–350 nm (center = 340 nm)

Band 4: 355–410 nm (center = 380 nm)

Band 5: 415–730 nm (center = 420 nm)

The centered value of each band is used to calculate the various cross section. For bands 1 and 2, ozone absorption and Rayleigh scattering are important and bands 4 and 5 are important for NO_2 absorption. Thus, results concerning band 2 (320 nm) and band 5 (420 nm) are discussed here. Calculations are performed for each band with SHDOM to generate a 3-D enhancement factor of the actinic flux integrated over each spectral band.

4.1. CLEAR SKY CONDITIONS

A simulation is performed with SHDOM to provide a profile of the actinic flux for 3 zenith angles (θ) in the cloud domain under clear sky conditions. The ground albedo is set to 0.05. Aerosols are not included in the radiative calculations.

In Figure 4, the enhancement factor versus altitude of the spectral actinic flux for bands 2 and 5 are plotted for 3 zenith angles. Results show that for overhead sun, the actinic flux is enhanced by a factor of 1.3 due to Rayleigh scattering (there is a strong diffuse component at low altitudes). At the ground, the low albedo (0.05) does not allow a significant upward diffused flux so the actinic flux is decreasing for both wavelengths. Also, the higher zenith angle is, the weaker the averaged value of the available actinic flux is. For 320 nm band, in the upper troposphere, this value decreases from 1.3 to 0.75 respectively for zenith angles $\theta = 0°$ and $\theta = 60°$ due mainly to the longer path length for ozone absorption. In these calculations, the total ozone column is taken from the McLafey atmospheric profile (283 Dobsons).

4.2. CLOUDY SKY ACTINIC FLUXES

In Figures 5(a, b) and 6(a, b), the total actinic flux enhancement factor (EF) calculated by SHDOM is shown in horizontal and vertical cross-sections of the cloud for an overhead sun. The distribution of the extinction coefficient within the cloud is also plotted and relate to the hydrometeor fields plotted in Figures 2 and 3.

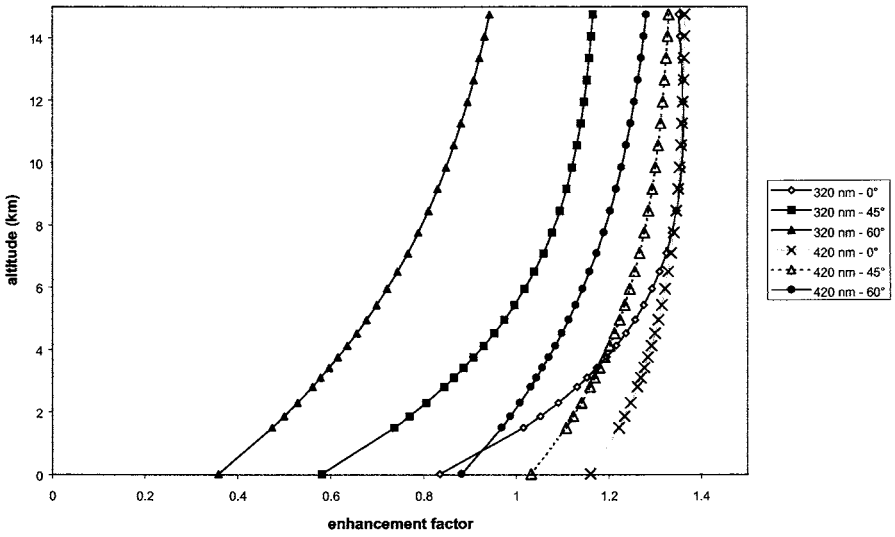

Figure 4. Enhancement factor (EF) of the actinic flux (AF) profile, under clear sky, for 320 nm and 420 nm bands for various zenith angles.

Horizontal cross-sections of EF at $z = 10.6$ km for 320 nm and 420 nm are shown in Figures 5(a, b), respectively. This altitude corresponds to the top edge of the anvil, and the extinction coefficient exhibit 3 maxima found over the 3 convective cells. The zero isoline for the extinction delimits the cloud shape. It can be seen that the cloud is at its mature stage with a large area occupied by the anvil. This is also confirmed by the vertical cross-sections across one cloud tower, at $Y = 40$ km (Figure 6). The anvil outflow begins at $z = 8$ km-altitude and the cloud (updraft) core extends horizontally over 10 km and vertically between 2–8 km. The extinction coefficient reaches a maximum of about 40 km^{-1} in the center of the tower, where hydrometeor concentrations are highest (Figures 2 and 3), and shows sharp gradients from the center to the edge where it decreases to 0.2 km^{-1}.

Outside and around the cloud, under clear air conditions, the EF is equal to 1.3 (see Figures 5(a, b), consistent with the clear sky results (Figure 4). The EF exhibits a maximum over each cloud tower. Averaged over the cloud, the EF is much smaller for 320 nm than for 420 nm, likely due to the fact that the ice crystals composing the anvil scatter more efficiently the 420 nm rather than the 320 nm spectral band; the difference can reach one order of magnitude. For 320 nm, the maximum is less pronounced (about 2.75) compared to 420 nm (max = 4.25). Using a simple approximation, Madronich (1987) has shown that the EF can be as high as 5 at the top edge of a cloud, and this is confirmed by our results. The EF vertical cross-sections plotted in Figures 6(a, b) respectively for 320 nm and 420 nm and for an overhead sun, clearly show the difference in magnitude for both wavelengths. Differences are also found at lower altitudes (outside and not under the cloud)

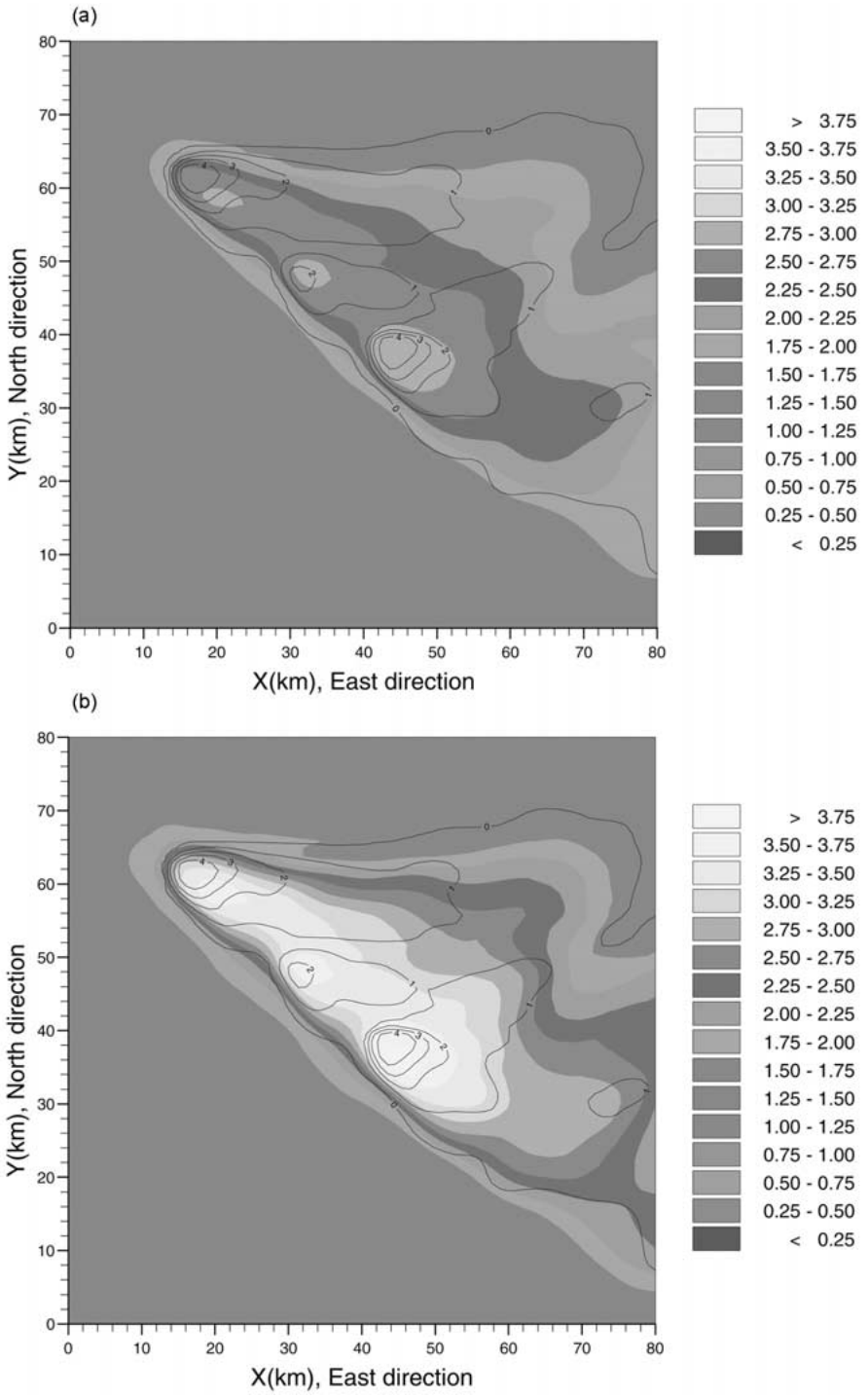

Figure 5. Horizontal cross-section of the EF, (a) 320 nm, $z = 10.6$ km, zenith $= 0°$ (isoline $=$ extinction); (b) 420 nm, $z = 10.6$ km, zenith $= 0°$.

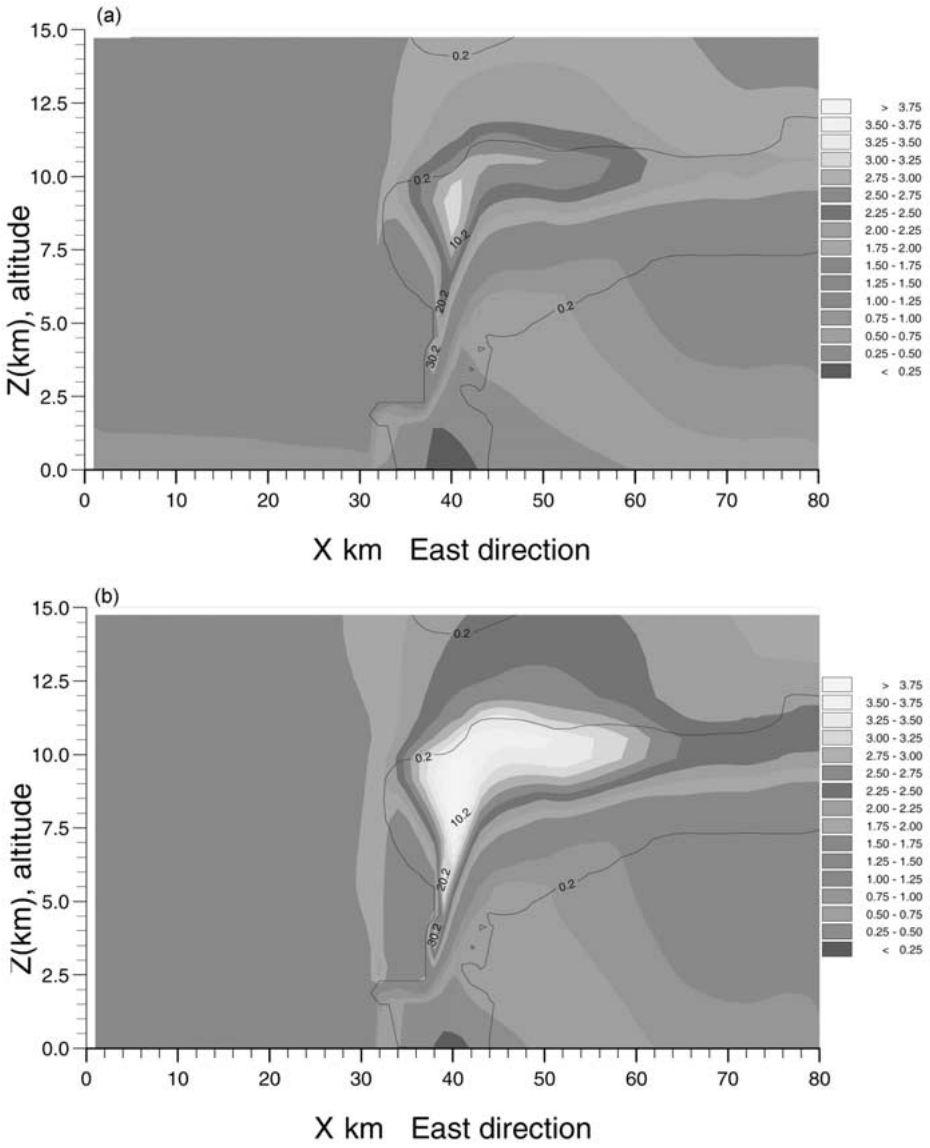

Figure 6. Vertical cross-section of the EF, (a) 320 nm, $y = 40$, zenith $= 0°$; (b) 420 nm, $y = 40$, zenith $= 0°$.

where the 320 nm case is altered more by the diffuse radiation leading to a vertical gradient of the EF (compare to the clear sky simulation). As an illustration, at 5 km, the EF (320 nm) is about 1.2 and at the ground less than 0.2, this is not observed for 420 nm.

These results show that for a convective cloud with a high spatial variability, the EF exhibits strongly inhomogeneous structure. At altitudes far above the anvil, the EF reaches a maximum of 2.8 for 420 nm and 2 for 320 nm at 15 km due to the cloud reflection. Because of deep convection, the actinic flux enhancement reaches the lower stratosphere, and the oxidizing capacity of the upper troposphere and lower stratosphere is modified.

In the lower part of the cloud, the low albedo specified for this simulation and the presence of thick clouds do not allow the propagation and intensification of the upward flux. This leads primarily to a darker sky for both wavelengths.

Zenith angles also effect the distribution of the actinic flux enhancement in the cloud domain. We present results for one wavelength (420 nm). Figure 7(a) corresponds to the zenith angle $\theta = 45°$, the solar radiation is coming from the left (or west) side of the cloud. Comparing the averaged EF between $\theta = 45°$ and $\theta = 0°$ (Figure 6(b)), it can be seen that the actinic flux decreases when θ increases. Above the cloud top, at 15 km, the EF is reduced to 1.5 for $\theta = 45°$ compared to 2.8 for $\theta = 0°$, at the same altitude. This lower EF is due to the lower intensity of the solar radiation and the less intense reflection at higher zenith angles at the top edge of the cloud. A larger EF is calculated along the left side of the cloud between 2.5 km and 5 km altitudes and $X = 30$ km to $X = 40$ km. This is due to the high concentration of cloud particles composed mostly of water droplets (Figure 3). This high value of the actinic flux calculated on the lateral cloud edge has a consequence on the EF in the clear air surrounding the cloud. Nevertheless, far from the cloud top, the clear air EF has the same magnitude as the EF calculated for a non-cloudy atmosphere including the Rayleigh scattering (see Figure 4).

For $\theta = 60°$ the situation is dramatically changed for the 420 nm wavelength (Figure 7(b)). The averaged EF is significantly reduced with a maximum less than 1.8. Two spots of large EF are found at the top of the cloud above a portion containing a large concentration of ice crystals, and also at lower altitudes near the left side of the cloud core. These results demonstrate that the actinic flux structure is 3-D in nature and is far from being homogeneous vertically or horizontally. The actinic flux distribution and intensity are very sensitive to the cloud spatial variability and microphysics. For 320 nm and 420 nm bands studied here, the dependency on zenith angle is obvious. For a lower sun, the 320 nm spectral band is absorbed more and has a lower EF compared to the 420 nm band.

In summer, deep convection occurs mostly in the afternoon, typically the frequency is maximum in the late afternoon and in early evening. The local time of the 10 July STERAO storm corresponds approximately to $\theta = 58°$. Because we intend to show the general impact of clouds on photolysis frequencies, the cloudy sky photolysis frequencies discussed in the next section are shown for $\theta = 0°$ and $\theta = 60°$; the latter corresponds to a more realistic situation for the time period of the day and location studied here.

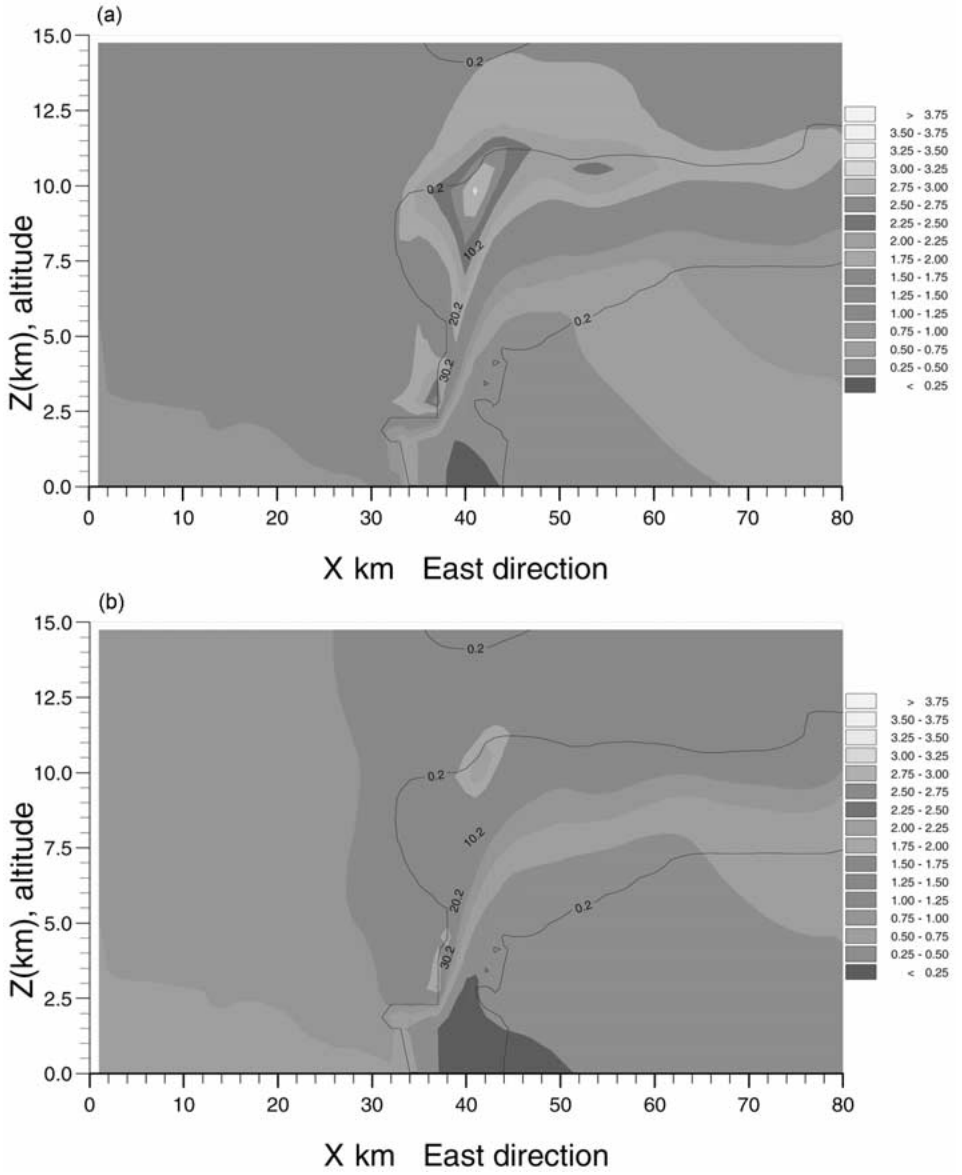

Figure 7. Vertical cross-section of the EF, (a) 420 nm, $y = 40$, zenith $= 45°$; (b) 420 nm, $y = 40$, zenith $= 60°$.

4.3. CLOUDY SKY PHOTOLYSIS FREQUENCIES

The calculation of photolysis frequencies requires a numerical integration of the photodissociation equation for each chemical species that depends on three parameters: the spectral distribution of their absorption cross-sections, the corresponding quantum yields (both of which are temperature-dependent), and the

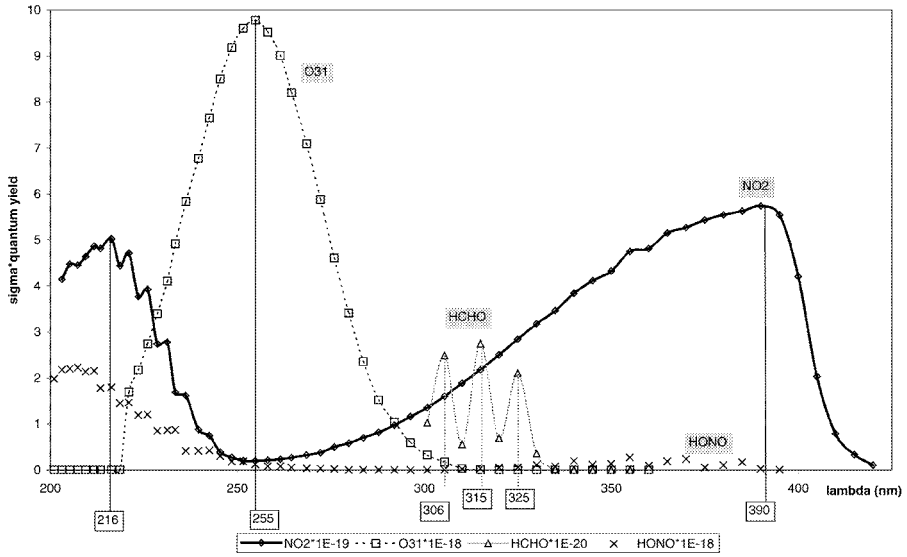

Figure 8. Absorption coefficient for various molecules function of wavelength.

available actinic flux. Chemical species do not necessarily absorb the solar flux at the same wavelengths. Also, frequently, the absorption cross sections are highly variable with respect to wavelength, so high spectral resolution is needed for the integrations. To calculate the absorption cross-sections and quantum yields, the spectral discretization are sufficiently high (171 intervals are specified over the solar spectra with a variable resolution in accordance with the importance of the spectral region) and the temperature dependence for all species is taken into account. However, the band method has been used for the actinic flux calculation as discussed previously.

As an illustration, the quantum yield and the cross-sectional products of some chemical species are plotted on Figure 8 assuming a fixed temperature (220 K). In The UT/LS, ozone is photodissociated into O^1D with the largest absorption occurring at 250 nm. The cross section of this species decreases sharply at 315 nm. Consequently, ozone is more sensitive to the EF distribution in band 2 (320 nm) than in band 5 (420 nm). In contrast to the ozone absorption, NO_2 absorbs the spectral wavelengths from 290 nm to 450 nm with a maximum around 380–400 nm. As a consequence, in the upper troposphere, NO_2 is rather sensitive to the EF distribution of bands 4 (380 nm) and 5 (420 nm).

In this work, absorption cross sections and quantum yields of various tropospheric and stratospheric chemical species are taken from De More *et al.* (1997) and Atkinson *et al.* (1994). As mentioned above, most of these species have an absorption coefficient dependent upon the temperature (Figure 9). Ozone photolysis frequency $J(O^1D)$ is highly correlated to air temperature; for tropopause conditions, where the temperature is low compared to the surface, $J(O^1D)$ is lower

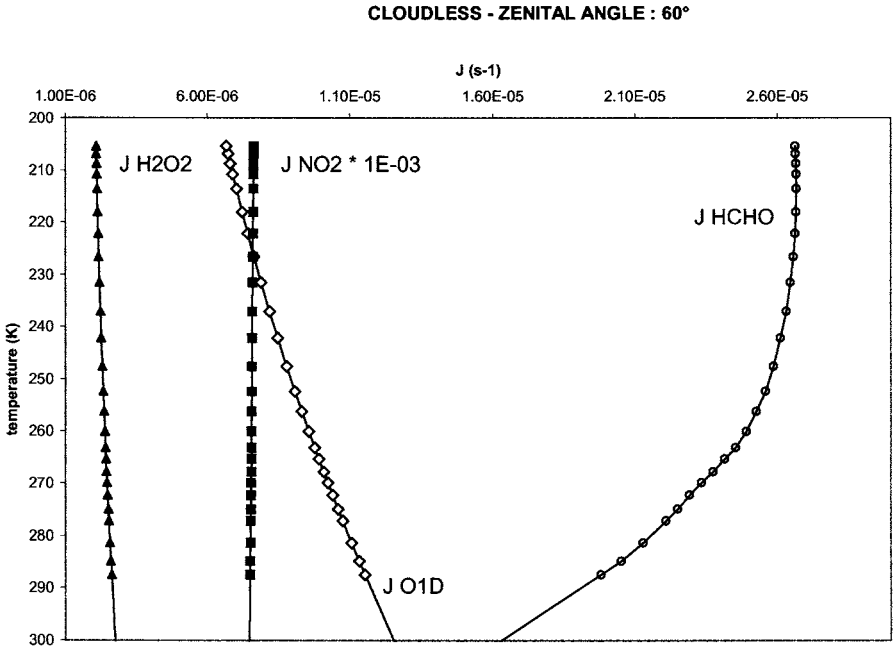

Figure 9. Temperature dependence of J's (see text).

than at the ground. J(HCHO) is negatively correlated with the temperature, and H_2O_2 and NO_2 are not very sensitive. The photochemical box model developed by Ramaroson (1989) includes the calculation of photolysis frequencies for these species and is adapted for this work. The three dimensional distribution of the actinic flux calculated by SHDOM is used by the model. The EF calculated in SHDOM and shown in earlier figures is simply multiplied by the corresponding incoming solar flux at the top of the cloud domain for the 5 spectral bands defined previously. It can be noted that the wavelength resolution used for SHDOM is not generally good enough to calculate photolysis frequencies, but it was chosen because of the computational demands of SHDOM.

In Figures 10(a, b), the vertical cross-section of $J(NO_2)$ at $y = 40$ km are plotted for the cloudy atmosphere and for a clear sky ($\theta = 0°$). The extinction coefficient is also given. As $J(NO_2)$ is not sensitive to the temperature (Figure 9), the vertical profile is similar to the variations of the actinic flux under clear air conditions (Figure 4). The minimum obtained near the ground is associated with the minimum in actinic flux available at this altitude. $J(NO_2)$ increases with altitude and reaches approximately 8×10^{-3} s^{-1} near the tropopause. This is probably lower than $J(NO_2)$ evaluated by other radiative models (Isaksen *et al.*, 1977). These differences could arise because of the magnitude of the incoming flux intensity specified at the top of the model domain. Figure 10(a) shows the $J(NO_2)$ cross-section for $y = 40$ km and $\theta = 0°$. Far from the cloud edge, $J(NO_2)$ exhibits the same magnitude than the clear

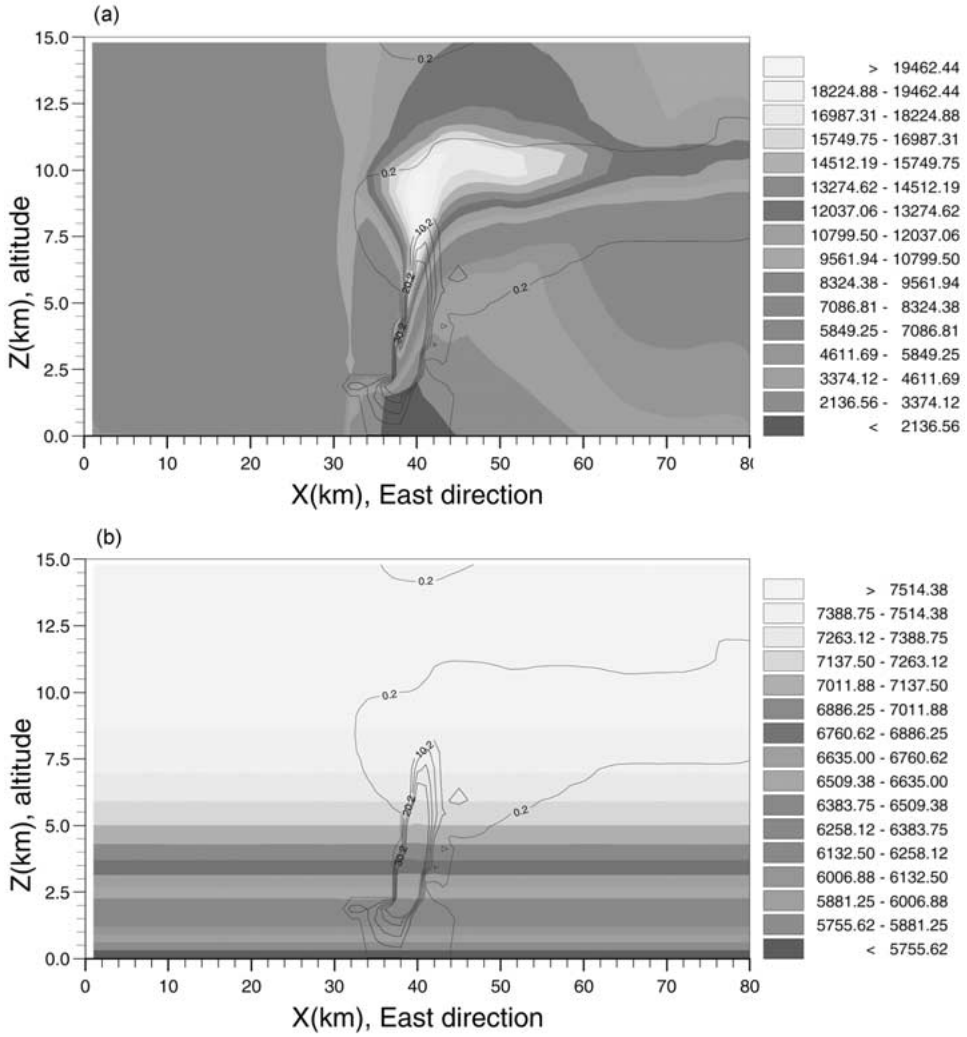

Figure 10. Vertical cross-section of JNO_2, $y = 40$, zenith $= 0°$; (b) clear sky.

air case (about 8×10^{-3} s^{-1}), consistent with the clear air actinic flux. Within the cloud and in the region where the extinction is largest, $J(NO_2)$ is about 2.5 times the clear air value. Above and outside the anvil, the cloudy/clear air ratio for $J(NO_2)$ is about 1.8. The shadow effect is under the cloud and is most pronounced just below the thick cumulus tower. The distribution of $J(H_2O_2)$ is similar to $J(NO_2)$ and is not discussed in this paper.

Figure 11(a) gives the cross-section of $J(O^1D)$ calculated under a cloudy atmosphere using the same temperature distribution as Figure 11(b). The temperature distribution (not shown here), used for clear and cloudy air is taken from the COMMAS model simulation, and the temperature decreases from the ground to

the tropopause with a deeper minimum over the top of the cloud due to the strong cooling at cloud top. Consequently, $J(O^1D)$ shows a minimum at the tropopause and increases above, as plotted in Figure 11(b). $J(O^1D)$ and temperature are positively correlated over the cloud domain; a minimum is found above the cloud top, a maximum is found in the cloud core where the temperature is much warmer (only the temperature is present and not the cloud). On the left side of the cloud, in the clean environment, the variation of $J(O^1D)$ with altitude is similar to Figure 11(b). In the upper half of the anvil, the cloudy/clear air ratio of $J(O^1D)$ is about 2.2. The anvil is thinner on the right side of the cloud, and the actinic flux penetrates deeper in the lower troposphere allowing enhanced photodissociation in contrast to below the cloud core where the shadow prevails (this is also true for $J(NO_2)$). Within and in the vicinity of the cloud, the effects of the temperature on $J(O^1D)$ is entirely masked by the large spatial variability of the actinic flux.

Cross-sections of J(HCHO), for the reaction HCHO $\rightarrow$ H + HCO, are plotted on Figures 12(a, b) for the cloudy sky and for clear air and for $\theta = 0°$. As shown in Figure 9, J(HCHO) is negatively correlated with the temperature between 300 and 270 K but is not sensitive to the temperature change between 260 K and 200 K. In Figure 12(b), the negative correlation with temperature is found in the lower and the middle troposphere. In the upper troposphere and lower stratosphere, J(HCHO) is generally correlated with the actinic flux distribution. In Figure 12(a), when the cloud is present, J(HCHO) exhibits a maximum similar to the EF above the cloud top. The ratio of cloudy/clear air J(HCHO) is equal to 2 at the same altitude where the $J(NO_2)$ ratio is 2.5. The reason that J(HCHO) is enhanced less than $J(NO_2)$ is that the two molecules absorb in different spectral regions. HCHO absorbs mainly in band 2, approximately between 300 nm and 335 nm, while NO_2 has strong absorption around 390 nm (spectral bands 4 and 5). As shown in the previous section, the EF is more efficient for band 5 than for band 2. Above the cloud and in the clear air near $z = 14$ km, the cloudy/clear air ratio for J(HCHO) is about 1.3 whereas for NO_2, it is 1.86 (for $J(O^1D)$ it is about 1.6).

As discussed previously, we have simulated the effects of the convective cloud on photolysis frequencies when the sun is at $\theta = 60°$, which corresponds approximately to the actual sun angle for the 10 July 1996 STERAO storm when the cloud was at its mature stage (late afternoon). The average value of $J(O^1D)$ plotted in Figure 13 is now reduced by a factor 2 (compared to an overhead sun), consistent with the actinic flux decrease at high zenith angle (versus low zenith angle) discussed in Section 4.2 (Figure 7(b)). The lateral effect is calculated over the top of the anvil in a small portion exposed directly to sun light (where a maximum of $J(O^1D) = 7 \times 10^{-6}$ s^{-1} is calculated).

The cross section of $J(NO_2)$ is plotted in Figure 14 for $\theta = 60°$. A maximum is found near the left side of the cloud, showing efficient multiple scattering in bands 4 and 5 (380 nm and 420 nm) and the significant energy available at these levels in these wavelengths. The $J(NO_2)$ in the clear air on the left side of the cloud is now stratified similar to that for an atmosphere without cloud (Figure 10(b)).

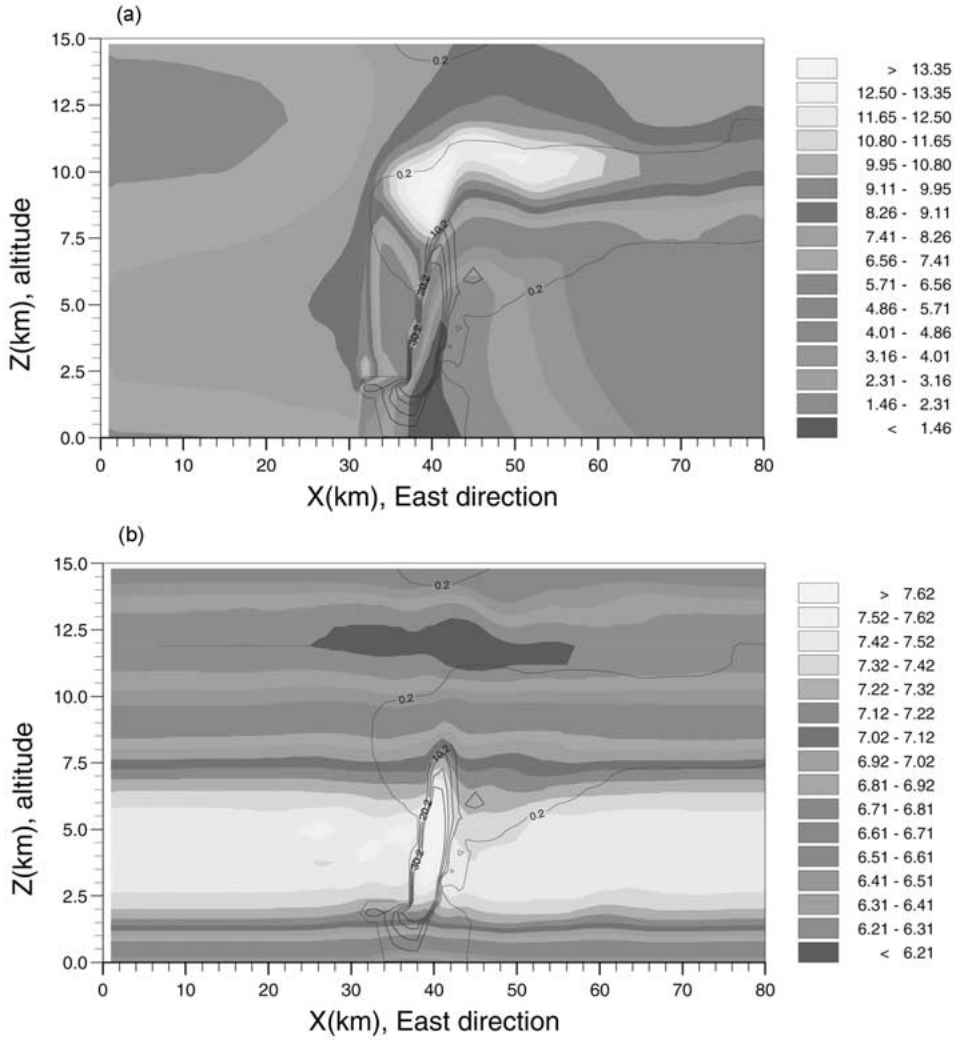

Figure 11. Vertical cross-section of $J(O^1D)$, $y = 40$, zenith $= 0°$; (b) clear sky.

In contrast to $J(O^1D)$, where the 320 nm is absorbed more and reduced at high zenith angle, the maximum $J(NO_2)$ is reduced only by a factor of 1.7 rather than by the factor 2 for $J(O^1D)$. The high spatial variability of the $J(NO_2)$ distribution is related to how the cloud microphysical species are handled in the radiative transfer calculation. The region of high $J(NO_2)$ in the anvil and along the solar ray direction corresponds to high ice crystal extinction.

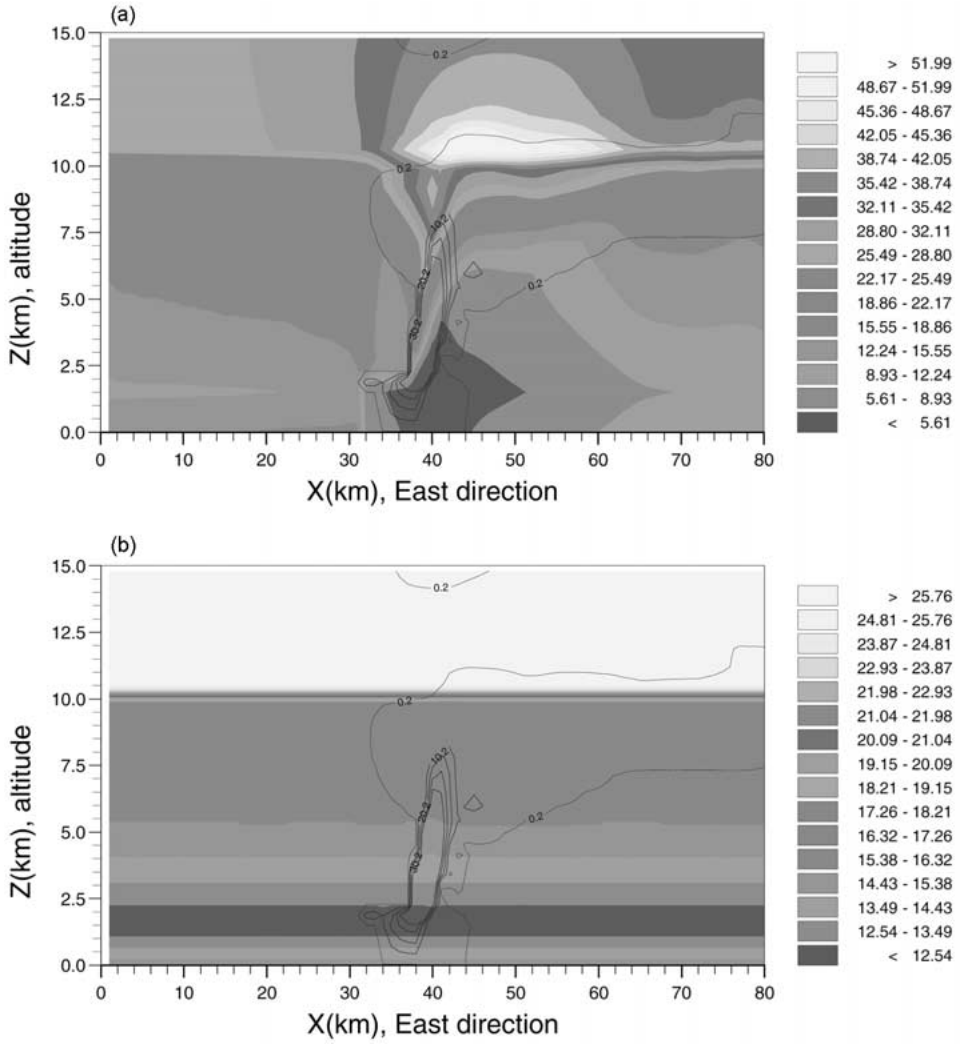

Figure 12. Vertical cross-section of JHCHO, $y = 40$, zenith $= 0°$; (b) clear sky.

5. Potential Impact of Clouds on Upper Troposphere and Lower Stratosphere Chemistry

It is clear that the regular presence of clouds in the troposphere would have a significant impact on the radiative budget (climate) and on photochemistry (atmospheric composition) in the upper troposphere and lower stratosphere. The IPCC special report (1999) concluded that ozone chemistry and transport processes near the tropopause are still affected by large uncertainties (e.g., the role of OH in oxidizing greenhouse gases and in regulating the ozone photochemistry). Among these uncertainties, the actinic flux distribution in the troposphere in the presence of clouds is poorly explored by model simulation and calculation with global or mesoscale

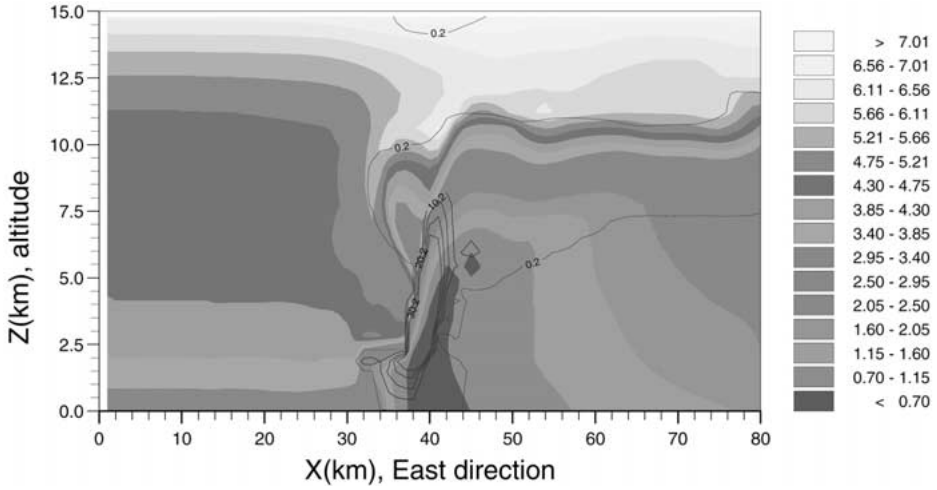

Figure 13. Vertical cross-section of J(O^1D), $y = 40$, zenith $= 60°$.

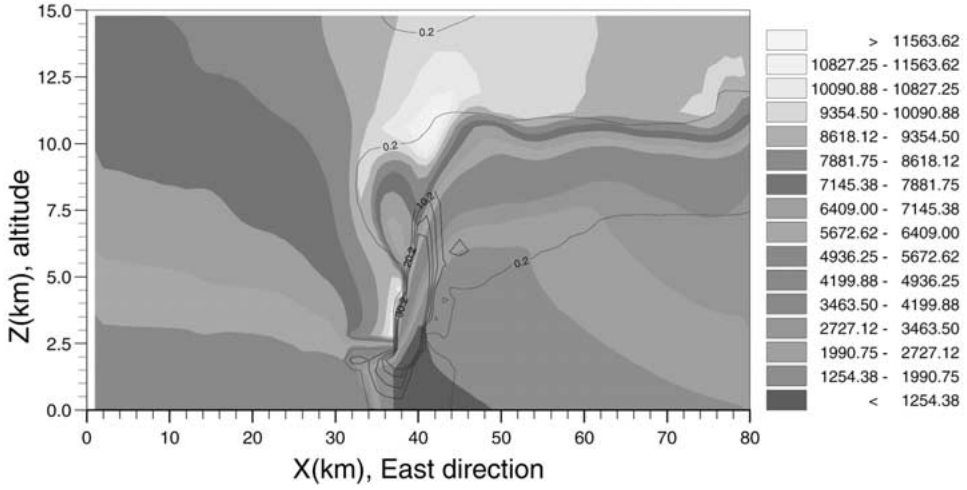

Figure 14. Vertical cross-section of J(NO_2), $y = 40$, zenith $= 60°$.

cloud observations are needed. In Section 4, we calculated the actinic flux transfer in a cloudy atmosphere and the high spatial variability of the impact of clouds on photolysis frequencies of molecules. To better understand the cloud effects on photolysis rates in mesoscale and global models, it is necessary to take into account the time variations of the photolysis rates over the globe. This likely will require the generation of a 4 dimensional look-up table containing the photodissociation of molecules versus time and space. For mesoscale and global models, this may prohibitively expensive when such a model simulation performed in this work is used.

In order to understand and quantify the potential influence of enhanced actinic fluxes on photochemistry around the tropopause, sensitivity studies are conducted by performing box model simulations (Ramaroson, 1989). The chemical simulations are performed in order to quantify the 'quasi-steady state' chemical response of the upper troposphere associated with the actinic flux enhancement previously calculated at the top of the anvil, at the lateral edges of the anvil and far above the cloud domain. The calculations are performed at different NO_x levels.

The chemical mechanism used in the box model derives from the 'Master Chemical Mechanism' (MCM, Derwent *et al.*, 1998). The mechanism describes the chemistry of the troposphere and the stratosphere and includes 190 species and 600 chemical reactions; no lumped method is used for the hydrocarbon chemical cycles. For hydrocarbon oxidation, all radical and derivative concentrations are calculated by the chemical solver. Because the number of species in MCM is prohibitive and inapplicable for 3-D mesoscale or global models, we include only the derivatives of C_2 to C_6 hydrocarbons such as alkanes, alkenes (propene and ethene), dialkenes (such the 3 ways of isoprene), alkynes (ethyne C_2H_2), and ketones. Heavier hydrocarbons are not taken into account; we assume that their lifetime is too short to allow their transport to the upper troposphere.

For specified non-methane hydrocarbon (NMHC) concentrations, box model simulations are performed until a 'quasi-steady state', averaged over the diurnal cycle, is reached. Long-lived species (e.g., CO) are allowed to vary during the integration. Photolysis frequencies are pre-calculated at finite zenith angles that depict the full day for two conditions. The clear sky condition includes photolysis rates that are not affected by clouds enhancing the actinic flux. The cloudy sky condition calculates the photolysis frequencies for continuous enhanced actinic flux conditions (corresponding to a grid point in the cloud domain where the maximum actinic flux enhancement factor occurred). Atmospheric conditions are chosen to be at the subsonic aircraft cruise levels ($z = 10.6$ km) at mid-latitudes (latitude = 40° N).

In Figure 15, the ozone production rates are plotted for both conditions as a function of the NO_x mixing ratio. For a clear sky, this production reaches a maximum of 2.9 ppbv/day for $NO_x = 300$ pptv and decreases when the NO_x mixing ratio increases. For a cloudy sky, the maximum ozone production rate is calculated for $NO_x = 500$ pptv, and a 14% difference is found between the cloudy and clear sky ozone production rates, whereas a 35% difference is obtained for $NO_x = 1.5$ ppbv.

The variations of the noon concentration of OH versus the integration time, for the clear and cloudy atmosphere and for two different NO_x concentrations, are plotted in Figure 16. For all conditions, OH reaches a maximum on the first day of the integration. This maximum appears to be a temporary adjustment to the initial conditions. After 10 days of integration, the OH mixing ratio at noon when cloud is present is about 75% greater than the OH mixing ratio without cloud for $NO_x = 400$ pptv and over two times greater for $NO_x = 1$ ppbv. These higher OH

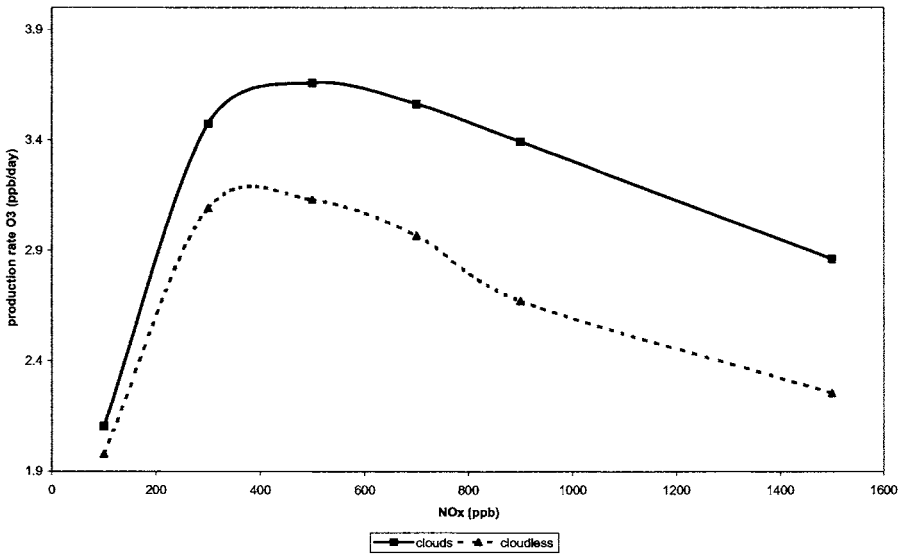

Figure 15. Ozone production rate versus NO_x, clear sky (dotted line), above cloud (full line).

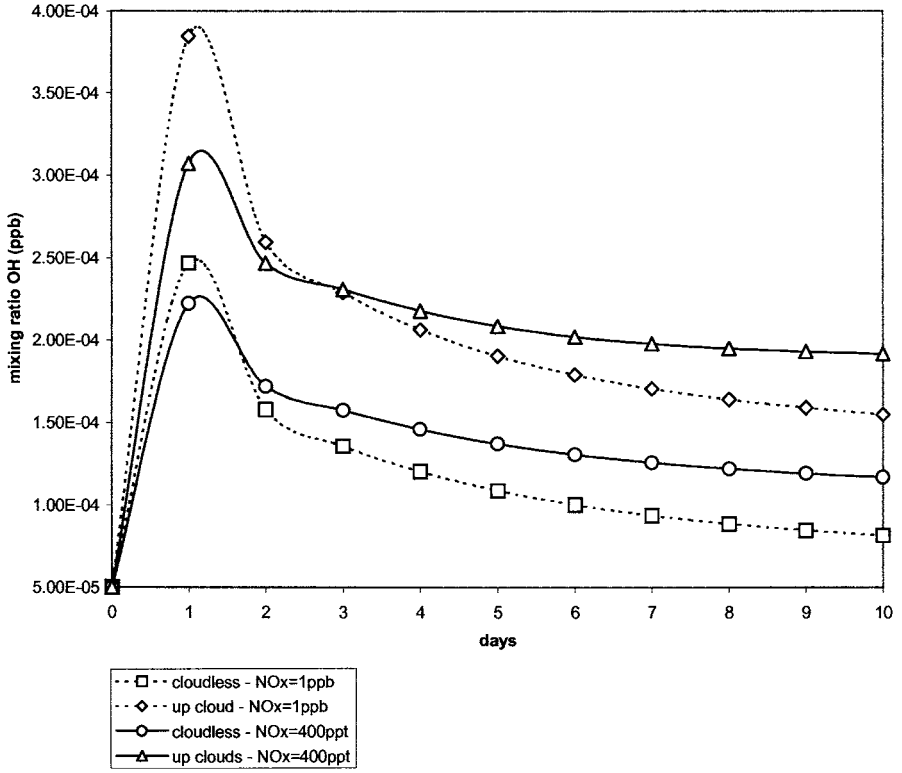

Figure 16. OH mixing ratio versus time for various NO_x, under clear sky and above cloud.

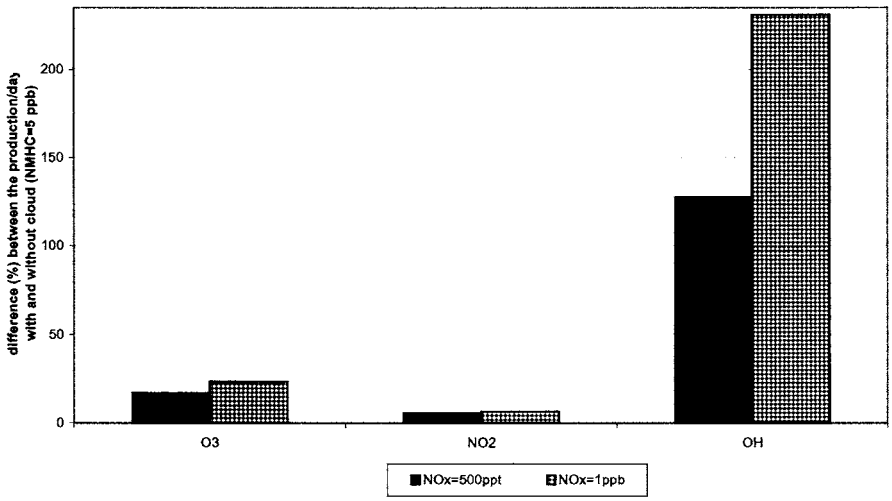

Figure 17. Percent change of production rate above cloud versus clear sky (O_3, NO_2, OH), for $NO_x = 0.5$ ppbv and 1 ppbv.

mixing ratios are on the same order and greater than the enhancement found in the photolysis frequencies of cloudy skies to clear skies for O_3, HCHO, and H_2O_2 photolysis. These photolysis reactions all produce HO_x while the major loss has not changed (oxidation of hydrocarbons). This striking effect on OH mixing ratios is also noted when comparing the difference in production rates between cloudy and clear air for OH, O_3 and NO_2 at two background NO_x mixing ratios and for NMHC = 5 ppbv (Figure 17). These results show that OH is most sensitive to the actinic flux distribution in the upper troposphere where the relative increase over clear sky conditions can reach 200% while the difference for ozone is about 30% and less than 10% for NO_2.

All of these results imply the necessity of a correct description of the actinic flux in the upper troposphere and lower stratosphere under all conditions in order to better describe the oxidizing capacity of these regions.

Thompson and Stewart (1991) showed that uncertainties of photochemistry frequencies introduce significant imprecisions and variations in chemical species concentrations. Our results showed that the presence of clouds implies an actinic flux enhancement factor. Photolysis frequencies depend on the actinic flux. Thus actinic flux variations involve photolysis frequencies variations and so tropospheric species variations.

6. Conclusion

We have demonstrated that clouds play an important role in the distribution of the total actinic flux in the troposphere and lower stratosphere. The spatial variability of the actinic flux distribution is correlated to the spatial inhomogeneities of the

cloud characteristics. Cloud microphysics is a key factor determining the absolute actinic flux enhancement due to multiple scattering in and around clouds. The Mie scattering related to water droplets can be described with sufficient precision, but uncertainties remain in the parameterization of ice crystal radiative characteristics because of the variations in shape, concentration, distribution, and phase function of the ice crystals. Near the top edge of the storm, the actinic flux (AF) is enhanced by a factor of 2–5, compared to the incoming flux at the top of the model domain. The enhancement depends on the extinction coefficient associated with the cloud microphysics. The actinic flux has local maxima above optically thick portions of the cloud and depends upon the solar zenith angle. For a low sun, it has been found that photolysis frequencies of molecules absorbing near 320 nm (such as O_3 and HCHO) are less sensitive to cloud effects as measured by the ratio cloudy air to clear air and compared to species that absorb at longer wavelengths (380–420 nm) such as NO_2. In addition, small wavelengths ($<$320 nm) are absorbed more by ozone at the tropopause and above inducing a lower available solar flux. The temperature effects were also considered. For clear air, overhead sun conditions, ozone photolysis to O^1D, $J(O^1D)$, exhibits a positive correlation with the atmospheric temperature and therefore has a minimum at the tropopause. This structure is completely masked by the presence of clouds for an overhead sun but remains in the clear air far from the cloud. However, for a low sun, this effect disappears and the $J(O^1D)$ profile is similar to the altitude variations of the actinic flux. No temperature dependency was calculated for NO_2. This species shows the most sensitivity to the actinic flux enhancement because NO_2 absorbs mainly at 420 nm. We can conclude that the determination of the actinic flux distribution in the troposphere and in the lower stratosphere is far from simple and requires additional model studies supported by local measurements, especially for high level clouds containing ice crystals.

The cloud effects on photolysis rates and on the chemistry around the tropopause have been explored for OH and ozone with respect to the background NO_x. Box model simulations have been performed to better understand and describe the potential impact of clouds on these species. It is found that the actinic flux enhancement at the top edge and above the cloud leads to a larger production of OH and ozone in the upper troposphere. We showed that the production of OH is always positively correlated to the actinic flux change in contrast to NO_x emission effects for which at a quasi-steady state, the ozone production is sufficient to increase the chemical losses of OH, and a net loss of OH is consequently obtained. These results imply the necessity of taking into account, in mesoscale or global scale models, the regular presence and effects of high, mid- and low level clouds.

Because photolysis frequencies are greatly modified by the presence of clouds, their effect should be included in large-scale chemistry and climate models so that better estimations can be made of the lifetimes of greenhouse gases and the impact of aircraft emissions on the upper troposphere and lower stratosphere chemistry. In addition, if climate radiative feedbacks induce greater persistence and/or greater

frequency of clouds, then the feedback via photolysis frequencies on tropospheric chemistry needs to be assessed (e.g., indirect impact of photolysis frequencies on CH_4 due to increased OH).

References

Atkinson, R., Baulch, D. L., Cox, R. A., Hampson, R. F., Kerr, J. A., and Troe, J., 1992: Kinetic and photochemical data for atmospheric chemistry, *J. Phys. Chem. Ref. Data* **21** (6), 1148–1315.

Chandrasekhar, S., 1960: *Radiative Transfer*, Dover, New York, pp. 1–4.

Claveau, J. and Ramaroson, R., 1996: First simulation of the transport and the chemical transformation of chemical species with a mesoscale-regional model: MEDIUM, in *International Colloquium on Effects of Aircraft upon the Atmosphere*, Paris, France.

Crawford, J., Davis, D., Chen, G., Shetter, R., Müller, M., Barrick, J., and Olson, J., 1999: An assessment of cloud effects on photolysis rate coefficients: Comparison of experimental and theoretical values, *J. Geophys. Res.* **104**, 5725–5734.

Crutzen, P., 1973: A discussion of the chemistry of some minor constituents in the stratosphere and troposphere, *Pure Appl. Geophys.* **106**, 1385.

DeMore, W. B., Sander, S. P., Golden, D. M., Hampson, R. F., Kurylo, M. J., Howard, C. J., Ravishankara, A. R., Kolb, C. E., and Molina, M. J., 1997: Chemical kinetics and photochemical data for use in stratospheric modeling, JPL publication 97-4, Evaluation nr. 12.

Derwent, R. G., Jenkin, M. E., Saunders, S. M., and Pilling, M. J., 1998: Photochemical ozone creation potentials for organic compounds in northwest Europe calculated with a master chemical mechanism (MCM), *Atmos. Environ.* **32**, 2429.

Evans, K. F., 1998: The spherical harmonics discrete ordinate method for three-dimensional atmospheric radiative transfer, *J. Atmos. Sci.* **55**, 429–446.

Finlayson-Pitts, B. J. and Pitts J. N., 1986: *Atmospheric Chemistry: Fundamentals and Experimental Techniques*, Chap. 3, Wiley-Interscience, New York, pp. 93–206.

Josefsson, W. and Landelius, T., 2000: Effect of clouds on UV irradiance: As estimated from cloud amount, cloud type, precipitation, global radiation and sunshine duration, *J. Geophys. Res.* **105**, 4927–4935.

Isaksen, I. S. A., Midtbo, K. H., Sunde, J., and Crutzen, P. J., 1977: A simplified method to include molecular scattering and reflection in calculations of photon fluxes and photodissociation rates, *Geophys. Norv.* **31**, 11–26.

Kelley, P., Dickerson, R. R., Luke, W. T., and Kok, G. L., 1995: Rate of NO_2 photolysis from the surface to 7.6 km altitude in clear-sky and clouds, *Geophys. Res. Lett.* **22** (19), 2621–2624.

Liou, K. N., 1980: *An Introduction to Atmospheric Radiation*, Academic Press, San Diego, U.S.A.

Liou, K. N. and Rao, N., 1996: Radiative transfer in cirrus clouds. Part IV: On cloud geometry, inhomogeneity, and absorption, *J. Atmos. Sci.* **53**, 3046–3065.

Logan, J. A., Prather, M. J., Wofsy, S. C., and McElroy, M. B., 1981: Tropospheric chemistry: A global perspective, *J. Geophys. Res.* **86**, 7210.

Los, A., van Weele, M., and Duynkerke, P. G., 1997: Actinic fluxes in broken cloud fields, *J. Geophys. Res.* **102**, 4257–4266.

Madronich, S., 1987: Photodissociation in the atmosphere 1-Actinic Flux and the effects of ground reflections and clouds, *J. Geophys. Res.* **92**, 9270–9752.

Madronich, S. and Weller, G., 1990: Numerical integration errors in calculated tropospheric photodissociation rate coefficients, *J. Atmos. Chem,* **10**, 289–300.

Matthijsen, J., Slaper, H., and Reinen, H. A. M., 2000: Reduction of solar UV by clouds: A comparison between satellite-derived cloud effects and ground-based radiation measurements, *J. Geophys. Res.* **105**, 5069–5080.

Platt, C. M., 1997: A parameterization of the visible extinction coefficient of ice clouds in terms of ice/water content, *J. Atmos. Sci.* **54**, 2083–2097.

Raïsänen, P., 1999: Effect of vertical resolution on cloud-sky radiation calculations: Tests with two schemes, *J. Geophys. Res.* **104**, 27407–27419.

Ramaroson, R., 1989: Local, one and three dimensional modeling of photochemical processes in the middle atmosphere, PhD thesis, Paris VI University, France.

Ramaroson, R., Pirre, M., and Cariolle, D., 1992: A box model for on-line computations of diurnal variations in multidimensional models: Application to the one-dimensional case, *Ann. Geophys.* **10**, 416–428.

Shetter, R. E. and Müller, M., 1999: Photolysis frequency measurements using actinic flux spectroradiometry during the PEM-Tropics mission: Instrumentation description and some results, *J. Geophys. Res.* **104**, 5647–5661.

Skamarock, W. C., Powers, J. G., Barth, M., Dye, J. E., Matejka, T., Bartels, D., Baumann, K., Stith, J., Parrish, D. D., and Hubler, G., 2000: Numerical simulations of the 10 July stratospheric-tropospheric experiment: Radiation, aerosols, and ozone/deep convection experiment convective system: Kinematics and transport, *J. Geophys. Res.* **105**, 19,973–19,990.

Takano, Y. and Liou, K. N., 1989: Solar radiative transfer in cirrus clouds. Part I: Single-scattering and optical properties of hexagonal ice crystals, *J. Atmos. Sci.* **46**, 3–19.

Tao, W-K. and Simpson, J., 1993: Goddard cumulus ensemble model. Part 1: Model description, *Terr. Atmos. Oceanic Sci.* **4**, 35–72.

Thompson, A. M. and Stewart, R. W., 1991: Effect of chemical kinetics uncertainties on calculated constituents in a tropospheric photochemical model, *J. Geophys. Res.* **96**, 13089–13108.

Trautmann, T., Podgorny, I., Landgraf, J., and Crutzen, P. J., 1999: Actinic fluxes and photodissociation coefficients in cloud fields embedded in realistic atmospheres, *J. Geophys. Res.* **104**, 30173–30192.

Turco, R. P., 1975: Photodissociation rates in the atmosphere below 1000 km, *Geophys. Surv.* **2**, 153–192.

Valero, F. P. J. and Bush, B. C., 1999: Measured and calculated clear-sky solar radiative fluxes during the subsonic Aircraft Contrail and Cloud Effects Special Study (SUCCESS), *J. Geophys. Res.* **104**, 27387–27398.

Van Weele, M., Vilà-Guerau de Arellamo, J., and Kuik, F., 1995: Combined measurements of UV-A actinic flux, UV-A irradiance and global radiation in relation to photodissociation rates, *Tellus*, serie B, **47**, 353–364.

Wicker, L. J. and Wilhelmson. R. B., 1995: Simulation and analysis of tornado development and decay within a three-dimensional supercell thunderstorm, *J. Atmos. Sci.* **52**, 2675–2703.